Applied Catalysis B: Environmental 140–141 (2013) 299–305

Contents lists available at SciVerse ScienceDirect

Applied Catalysis B: Environmental

journal homepage: www.elsevier.com/locate/apcatb

Erbium doped TiO_2–Bi_2WO_6 heterostructure with improved photocatalytic activity under sun-like irradiation

S. Obregón, G. Colón*

Instituto de Ciencia de Materiales de Sevilla, Centro Mixto CSIC-Universidad de Sevilla, C/Américo Vespucio, 49, 41092 Sevilla, Spain

ARTICLE INFO

Article history:
Received 15 February 2013
Received in revised form 2 April 2013
Accepted 4 April 2013
Available online 20 April 2013

Keywords:
Erbium
TiO_2
Bi_2WO_6
Photocatalysis
Solar-like

ABSTRACT

Erbium doped TiO_2–Bi_2WO_6 have been synthesized by means of a surfactant free hydrothermal method having good photoactivities under sun-like excitation for the degradation of Rhodamine B. From the structural and morphological characterization it has been stated that the presence of Er^{3+} induces a progressive russelite cell contraction due to its incorporation in the Bi_2WO_6 lattice in substitutional sites. The best photocatalytic performance was attained for the samples with 1 at% of Er. From the study of the photocatalytic activity under different irradiation conditions it can be inferred that Er^{3+} presence induces a significant improvement of the photoactivity in the UV range. The evolution of band-gap values seems to be similarly related with the reaction rate progression. Thus, the higher band-gap values in lower Er doped systems would be the cause of a better electron hole separation under UV irradiation.

1. Introduction

Heterogeneous photocatalysis technology is considered as a promising route to afford pollutant degradation as well as hydrogen production processes [1]. Nowadays, the research activity in this field is focused in the development of novel alternative materials to traditional TiO_2 capable to use of sunlight as the green energy source [2]. For this reason, use of visible light photons, but also an adequate overall handling of UV–vis radiation constitutes the key point for a good photocatalyst performance under sunlight conditions. A significant number of new photocatalysts do perform adequately under visible light but typically display poor performance with respect to TiO_2 commercial references (e.g., Degussa P25) under sunlight. This is due to an unfavorable balance between the enhanced visible light absorption and a negative impact on charge recombination [3]. For that reason, instead of using a single semiconductor, coupling of semiconductors with other semiconductors, metals, and molecules forming a junction structure has been found to enhance the photocatalytic performance by improving the charge carrier separation or enhancing the spectral absorption range [4–7]. Among these, doping of TiO_2 with hybrid atoms or coupling TiO_2 with other semiconductors with low band gaps have proved to be viable ways to allow the extension of light absorption edge [8,9]. An alternative option consists on the creation of new single phase visible active catalysts which would overcome the drawbacks of doping [10–14].

In this sense, the TiO_2–Bi_2WO_6 heterostructure has been demonstrated to be a promising strategy [9]. The optimized charge carrier dynamic performed by the conjunction of TiO_2 and Bi_2WO_6 was proposed to be the reason of the enhanced photoactivity of the system.

Moreover, we proposed the Er^{3+} doping into TiO_2 as host matrix [15]. We could state a double synergetic mechanism in which Er^{3+} ions participate in the overall photocatalytic process; On the one hand, by improving the electron–hole separation and on the other by coupling a cooperative luminescence process [16]. Thus, in the present paper we study the effect of erbium doping on the heterostructured TiO_2–Bi_2WO_6 system.

2. Experimental

2.1. Synthesis of photocatalysts

The Er^{3+}-TiO_2–Bi_2WO_6 samples were prepared by a hydrothermal method similar to that previously reported by us [9]. For this purpose, a certain amount of $Bi(NO_3)_3{\cdot}5H_2O$ (Sigma–Aldrich, ≥98.0%) was dissolved in 10 mL of glacial acid acetic at room temperature. A second aqueous solution was prepared by dissolving the corresponding stoichiometric ratio of $Na_2WO_4{\cdot}2H_2O$ (Sigma–Aldrich, ≥99.0%) and the appropriate amount of $Er(NO_3)_3{\cdot}5H_2O$ (Sigma–Aldrich, 98.9%) in 60 mL of distilled water. This aqueous solution was added to the bismuth nitrate solution and the process was accompanied with a vigorous

* Corresponding author. Tel.: +34 954489536.
E-mail address: gcolon@icmse.csic.es (G. Colón).

0926-3373/$ – see front matter
http://dx.doi.org/10.1016/j.apcatb.2013.04.014

stirring. Separately, a stock TiO_2 colloidal solution was prepared by means of a previously reported procedure [17]. Then, 0.5 mL of this TiO_2 colloidal solution (to achieve 5% of TiO_2 with respect to Bi_2WO_6) was added to the white Er,Bi-tungstate suspension. The pH of the final suspension was adjusted to 9 by adding triethylamine (TEA). The mixture was placed in a Teflon recipient inside of stainless steel autoclave reactor. The hydrothermal treatment was performed at 140 °C for 20 h. The as obtained precipitate was then cooled until room temperature, filtered and repeatedly washed and dried overnight at 120 °C. Afterwards, the powder was submitted to a further calcination treatment at 300 °C for 2 h. Samples will be named as BWO and TBWO for Bi_2WO_6 and TiO_2–Bi_2WO_6 respectively.

2.2. Materials characterization

BET surface area and porosity measurements were carried out by N_2 adsorption at 77 K using a Micromeritics 2010 instrument.

X-ray diffraction (XRD) patterns were obtained using a Siemens D-501 diffractometer with Ni filter and graphite monochromator. The X-ray source was Cu Kα radiation (0.15406 nm). Rietveld analyses were performed by using XPert HighScore Plus software over selected samples. The diffraction patterns were recorded from 2θ 10° to 120° with step of 0.017° and 400 s per step.

The chemical composition of the samples was determined by X-ray fluorescence spectrometry (XRF) in a Panalytical Axios sequential spectrophotometer equipped with a rhodium tube as the source of radiation. XRF measurements were performed on pressed pellets (sample included in 10 wt% of wax).

Micro-Raman measurements were performed using a LabRAM Jobin Yvon spectrometer equipped with a microscope. Laser radiation (λ = 532 and 780 nm) was used as excitation source at 5 mW. All measurements were recorded under the same conditions (1 s of integration time and 30 accumulations) using a 100× magnification objective and a 125 mm pinhole.

The morphology of samples was followed by means of field emission-SEM (Hitachi S 4800). The samples were dispersed in ethanol using an ultrasonicator and dropped on a copper grid.

UV–vis spectra (Shimadzu, AV2101) were recorded in the diffuse reflectance mode (R) and transformed to a magnitude proportional to the extinction coefficient (K) through the Kubelka–Munk function, $F(R\infty)$. Samples were mixed with $BaSO_4$ that does not absorb in the UV–vis radiation range (white standard). Scans range was 240–800 nm.

2.3. Photocatalytic experimental details

Rhodamine B oxidation reactions were performed using a batch reactor (250 mL) using an arc lamp source (Oriel Instruments) equipped with a Hg–Xe lamp of 200 W. The intensity of the incident UVA and visible light on the solution was measured with a HD2302 photometer (Delta OHM) using LP 471 UVA and LP 471 RAD sensors (spectral responses 315–400 nm and 400–1050 nm respectively). The intensity of the lamp under different irradiation conditions is summarized in Table 1. In the oxidation tests, an oxygen flow was employed what produces a homogenous suspension of the catalyst in the solution. Before each experiment, the catalysts (1 g/L) were settled in suspension with the reagent mixture for 15 min. The evolution of the initial Rhodamine B (*RhB*) concentration (ca. 10 ppm) was followed through the evolution of the characteristic 553 nm band using a centrifuged aliquot ca. 2 mL of the suspension (microcentrifuge Minispin, Eppendorf). In order to distinguish the different contributions of the different ranges of the lamp spectrum, UV–vis–NIR, UV–vis, vis–NIR and vis photocatalytic experiments were performed by using UV and IR cut-off filters (λ < 420 nm and λ > 800 nm respectively).

Table 1
Lamp irradiance (W/m^2) under different conditions.

Luxometer sensor	UV–vis–IR	UV–vis	vis–IR	vis
LP471 UVA (315–400 nm)	85	67	0.2	0.2
LP471 RAD (400–1050 nm)	542	209	482	163

3. Results and discussion

The single Bi_2WO_6 photocatalyst presents the russelite structure (PDF 79-2381 corresponding to the orthorhombic *Pca2₁* space group) (Fig. 1). Moreover, as previously reported by us, the TiO_2–Bi_2WO_6 heterostructure only exhibits the russelite structure without any evident traces of anatase [9]. We evidenced that TiO_2 incorporation is taking place in the Bi_2WO_6 structure causing a certain distortion in its unit cell. This fact would indicate that the incorporation of TiO_2 units would compress the layered structure. For erbium doped heterostructures it can be observed the same russelite crystalline structure (Fig. 1a). From Rietveld refinement, it is possible to ascertain that the presence of erbium leads to a slight progressive diminution of the cell volume (Fig. 1b). This cell contraction would evidence the incorporation of Er^{3+} in the russelite structure, probably substituting the bismuth ions. Similar effect was stated for Er^{3+} doped $BiVO_4$ for which a clear cell diminution of the tetragonal phase was associated with the substitution of Bi^{3+} by Er^{3+} [18]. From the evolution of the cell volume it can be noticed that the incorporation of Er^{3+} affect the cell volume till Er^{3+} content of 1 at%. After such doping the cell volume remains almost constant. This would imply that the incorporation into the russelite structure is taking place till loading is 1%, after which Er^{3+} probably would segregate. By observing the evolution of cell parameters it is clear that the slight cell volume shrinkage is caused by the shortening of a parameter (Fig. 1c). Thus, it can be noticed that a parameter decrease in much extent than b growing, while c parameter remains almost constant.

The crystallite sizes, calculated from the line width of (1 3 1) diffraction peak (Table 2), clearly show a great variation between BWO and TBWO (from 30 to 20 nm respectively). However, the incorporation of Er^{3+} does not induce a significant change in crystallite size and all heterostructures present similar crystallite size around 20 nm. For platelike Bi_2WO_6 particles, crystallite size calculated from (1 3 1) diffraction peak width has been associated with the average plate thickness [19]. Therefore, the obtained similarity in this value would indicate an analogous thickness.

The BET surface areas for the heterostructured Er-TBWO systems are shown in Table 2. It appears that the incorporation of TiO_2 clearly induces a notably increase in the surface area value. Moreover, as Er^{3+} is incorporated BET surface areas seems also to increase progressively, reaching a maximum value for 1 at% of Er^{3+} content. The erbium content obtained by XRF chemical analysis was

Table 2
Surface, structural and photocatalytic characterization for Er^{3+} doped TiO_2–Bi_2WO_6 catalysts.

Samples	Crystallite size (nm)	BET (m^2/g)	Band gap (eV)	Er^{3+} content (%)
BWO	30	9	2.91	–
TBWO	20	15	2.90	–
Er-TBWO				
0.50 at% Er^{3+}	20	15	2.90	0.5
0.75 at% Er^{3+}	21	14	2.96	0.8
1.00 at% Er^{3+}	18	17	2.97	0.9
1.25 at% Er^{3+}	19	16	2.95	1.3
2.00 at% Er^{3+}	20	14	2.91	2.2
4.00 at% Er^{3+}	19	15	2.92	4.3

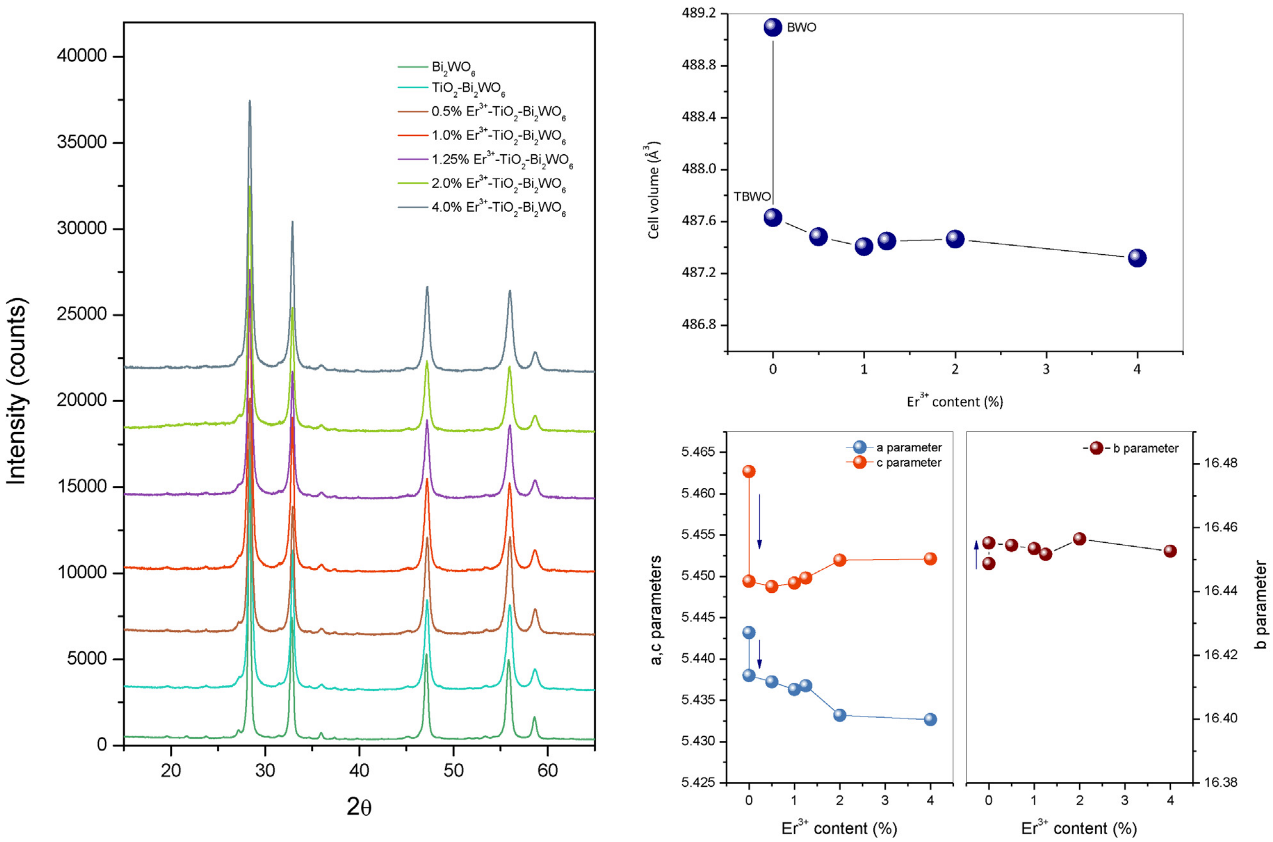

Fig. 1. (a) XRD patterns for Er^{3+}-TBWO catalysts; (b) evolution of the Bi_2WO_6 cell volume, and (c) evolution of the orthorhombic cell parameters with the increasing Er^{3+} content.

also shown in Table 2. It can be seen that erbium concentration reasonably fits with nominal values in all cases.

From the Raman spectra of BWO and TBWO it can be clearly evidenced the above assumption made from XRD results. No evidence of anatase bands can be detected in the Raman spectra for the heterostructured TBWO (see inset in Fig. 2a). Thus, both BWO and TBWO samples show the bands in the range 200–1000 cm^{-1} that can be assigned to Raman actives modes for Aurivillius $BiWO_6$ ($2A_1 + B_1 + 3E_g$) [20]. The bands located at 790 and 820 cm^{-1} have been associated with the symmetric and antisymmetric W—O stretching modes in WO_6 octahedra that involve motions of the apical oxygen atoms [21,22]. Similarly, bands around 700 cm^{-1} have been assigned to W—O stretching modes for equatorial oxygens of WO_6 octahedra. Finally, the bands in the 200–400 cm^{-1} region can be assigned to the bending vibration of WO_6 and stretching and bending vibration of BiO_6 polyhedra [21,22]. When erbium ion is present it can be observed the appearance of new a series of high intensity bands which completely overlap the bands of Bi_2WO_6 (Fig. 2a). Such bands could be associated with the luminescence processes from Er^{3+} ions in the tungstate structure upon excitation with green laser at 532 nm [23]. Raman spectra registered with red laser excitation allow us to distinguish the described bands corresponding to Bi_2WO_6. This would indicate that upon excitation at 780 nm the strong luminescence process observed is almost lost. From this result it can be pointed out that erbium incorporation does not induce any significant changes in the position of the Raman bands nor the presence of TiO_2, and induces a notably luminescence bands upon excitation at 532 nm.

Regarding the morphology, all samples show plate-like aspect of a few hundreds of nanometers and thicknesses of 20–30 nm, which is in accordance with crystallite size obtained from Scherrer equation (Fig. 3). As previously reported, the morphology of Bi_2WO_6 is rather sensitive to the preparation conditions, showing flower-like hierarchical organization due Ostwald ripening process when the pH of the preparation is low [24]. In our case the ripening process is not present. The morphology of the microplates experiments a slight change for erbium doped heterostructures. Thus it can be noticed the aggregation of particles accompanied with a certain diminution of the plate size.

The absorption properties of the studied photocatalysts are reported in Table 2. As it can be noticed, the TBWO system present similar band gap values as BWO. So, the band-gap values are similar and close to 2.89 ± 0.2 eV which is the typical reported for Bi_2WO_6 [25]. Erbium doped heterostructures do not show a different absorption feature with respect to the undoped one (Fig. 4). Nevertheless, it can be noticed that the band-gap values slightly increases, reaching a maximum value of 2.97 ± 0.2 eV for 1 at% doped sample. Moreover, it can be observed in the visible region small absorption bands corresponding to the excitation of Er^{3+} species [26]. These absorption lines located at 523 and 653 nm would correspond to the transitions from the Er^{3+} ground state $^4I_{15/2}$ to the higher energy levels $^4H_{11/2}$ and $^4F_{9/2}$ respectively [15].

In Fig. 5 we show the photocatalytic behavior of BWO, TBWO and erbium doped TBWO systems. The photocatalytic activity of the TBWO composite structures clearly denotes an improved performance with respect BWO system. This effect was already stated by us and was explained in terms of a synergetic effect between both semiconductors [24]. Furthermore, as previously reported, the predominant degradation mechanism observed for TBWO systems is based on the N-deethylation in spite of chromophore cleavage [27]. In addition, heterostructured TiO_2–Bi_2WO_6 catalysts have clearly showed high mineralization rates, indicating that not only discoloration but degradation have been achieved. The intimate conjunction of TiO_2 and Bi_2WO_6 would be the

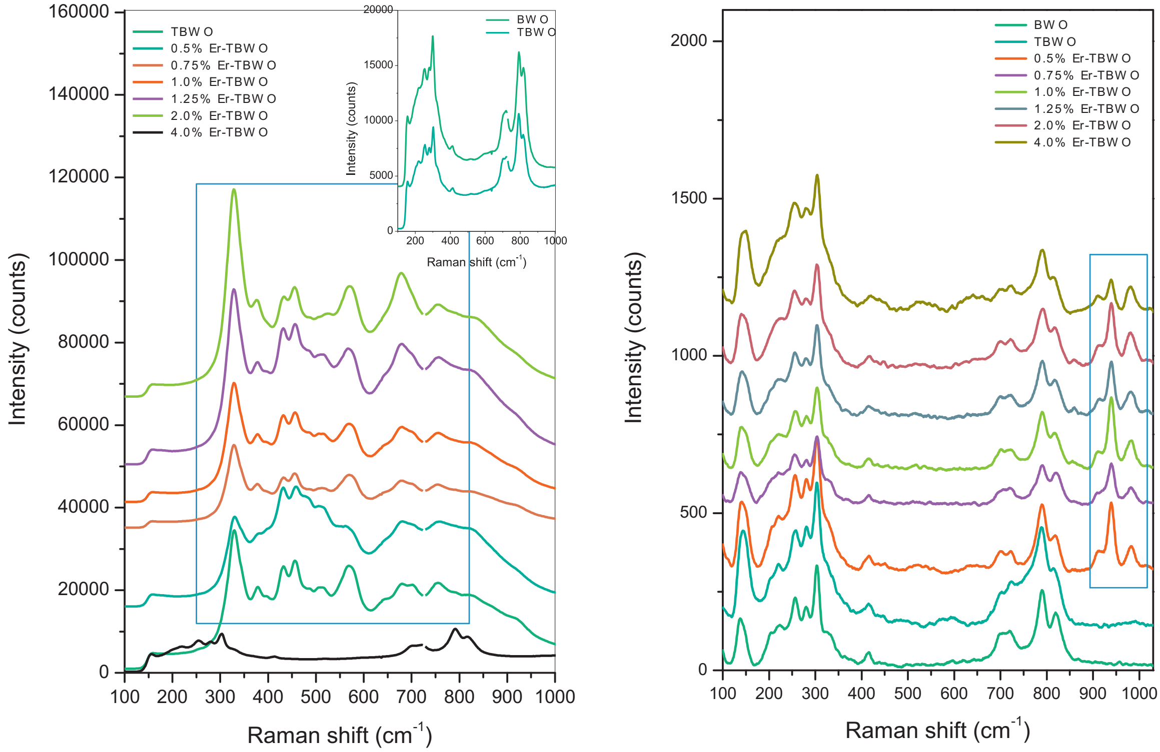

Fig. 2. Raman spectra for Er^{3+}-TBWO catalysts upon (a) green laser excitation at 532 nm; (b) red laser excitation (780 nm). (For interpretation of the references to color in this figure legend, the reader is referred to the web version of the article.)

reason of the optimized charge carrier dynamic that would lead to the enhanced photoactivity of the heterostructured system.

As it can be seem, the incorporation of erbium clearly produces a noticeable improvement of the photoactivity, achieving to the complete disappearance of *RhB* after 1 h of illumination for 1 at% of Er doped TBWO system. Thus, the reaction rates clearly experiment a progressive rise as dopant content increases. This improving effect takes place till Er^{3+} loading is 1 at%. Since Er-TBWO samples exhibit slightly higher surface area values (Table 1), we have

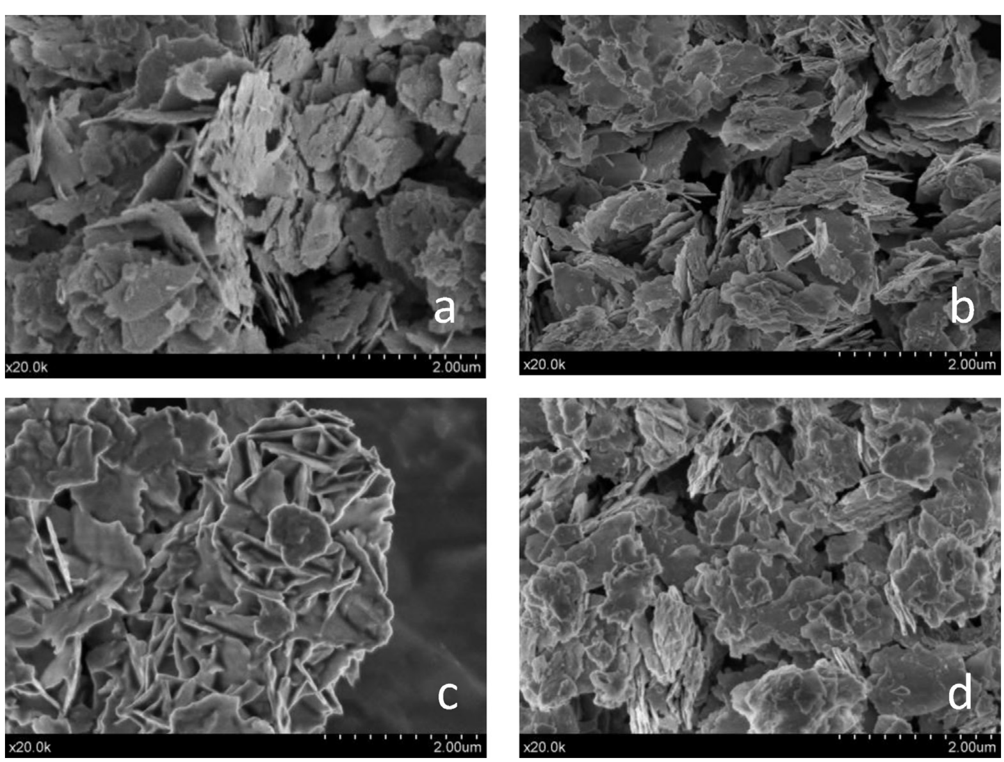

Fig. 3. FE-SEM images of (a) TBWO, (b) Er^{3+}-TBWO (0.75 at%); (c) Er^{3+}-TBWO (2.0 at%) and (d) Er^{3+}-TBWO (4.0 at%) heterostructures.

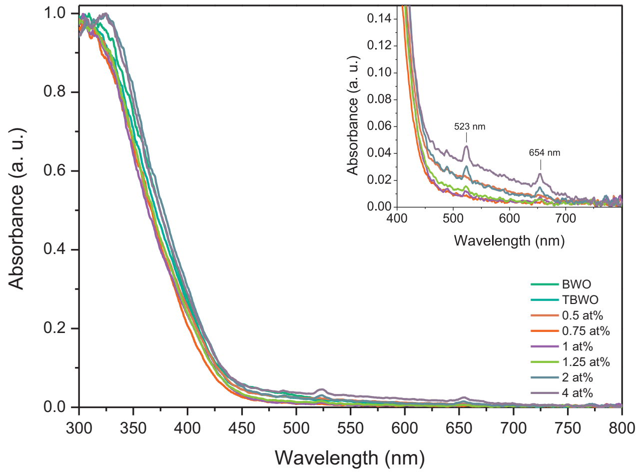

Fig. 4. Diffuse reflectance spectra for Er^{3+} doped TBWO systems.

represented the specific reaction rate per surface area unit (Fig. 5c). Thus, we could separate the influence of surface area in the reaction rate. As it can be noticed, Er-TBWO samples still show better photocatalytic performance per surface area unit, reaching in this case the maximum photoactivity for 0.75 at% doped system. Therefore we may assess that Er doping produces a notably enhancement of the photocatalytic activity by both increasing the surface area of the photocatalysts as well as by participating in the overall photocatalytic mechanism.

In order to elucidate the specific role of erbium on the reaction mechanism, we have performed the degradation reaction under different irradiation conditions (Fig. 6a–c). The photoactivities under both UV–vis and visible irradiation appear somewhat improved for the heterostructures, reaching the complete *RhB* disappearance around the first 60 min of illumination. By observing the reaction rates calculated from the conversion plots it appears that reactions performed under vis and vis–NIR exhibit similar conversion plot for TBWO and Er-TBWO (Fig. 6d). However, under UV–vis irradiation, erbium doped heterostructure presents a noticeable enhancement. From this result it can be assumed that

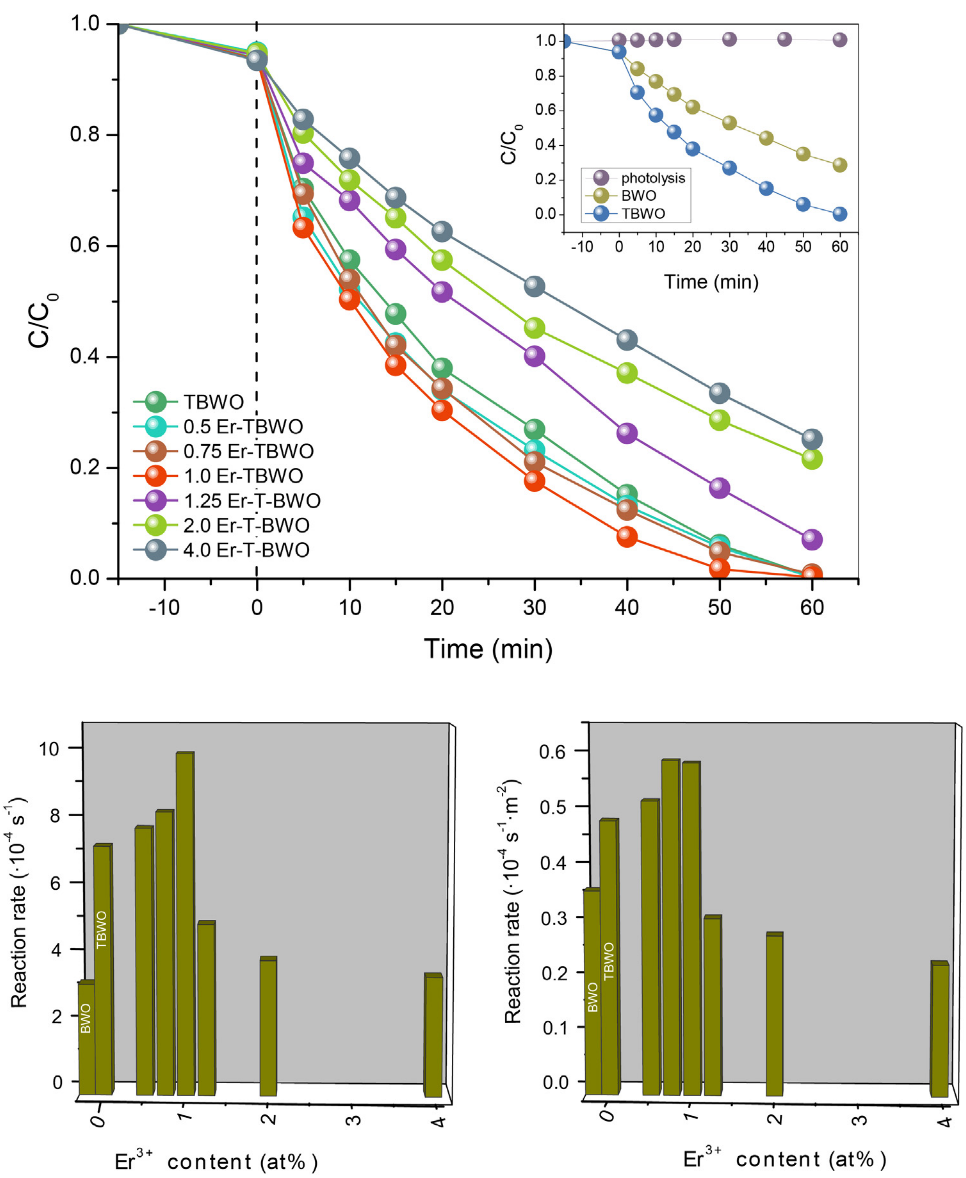

Fig. 5. (a) Evolution of *RhB* with photodegradation time for different Er^{3+}-TBWO photocatalysts; (b) variation of the reaction rate, and (c) reaction rate per surface area unit with Er^{3+} content under UV–vis–NIR full lamp spectrum.

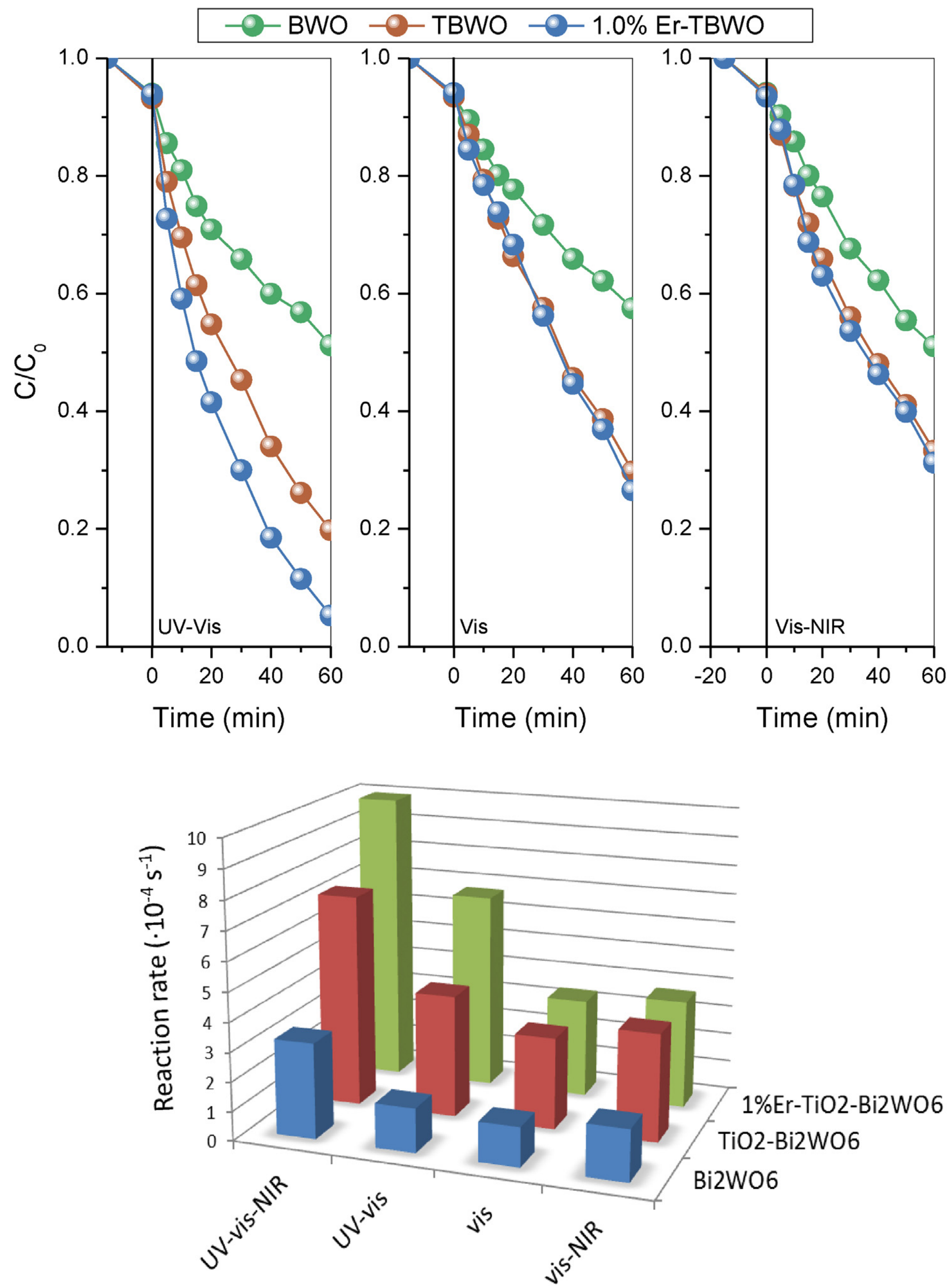

Fig. 6. (a) Evolution of *RhB* with photodegradation time for different Er^{3+}-TBWO photocatalysts; (b) variation of the reaction rate, and (c) reaction rate per surface area unit with Er^{3+} content under different spectral lamp ranges.

erbium would affect to the electronic mechanism under UV excitation. If we consider the evolution of band-gap values, it can be pointed out a similar evolution as photoactivity. We might infer that the higher the band-gap, the higher the reaction rate. If take into account the proposed mechanism reported by TiO_2–Bi_2WO_6 heterostructure, it can be assumed that under UV the effective charge separation would be the responsible of the improved photoactivity [24]. Thus, for Er doped TBWO the slightly higher band gap values would represent a higher driving force for electron–hole separation (Scheme 1). In fact, from calculated band-gap values it is possible to obtain empirically the conduction band energy [28]. Although the band edge positions are not easily determined experimentally, a theoretical prediction is possible using concepts of Mulliken electronegativity. Thus, the conduction band edge energy of a semiconductor at the point of zero charge can be expressed by

$$E_{CB} = \overline{\chi} - E_e - \frac{E_g}{2}$$

where E_{CB} is the conduction band edge potential, χ is the Mulliken electronegativity of the semiconductor (which is the geometric mean of the electronegativities of the constituent atoms), E_e is the energy of free electrons on the hydrogen scale (4.5 eV) and E_g is the band gap energy of the semiconductor. By using this approximation we have estimated the values for E_{CB} and E_{VB} (Fig. 7). By observing the evolution of both band edges it is possible to assume that Er^{3+} induces a slight modification of band positions. Such small shift, denoted by the band gap value enlargement, clearly affects

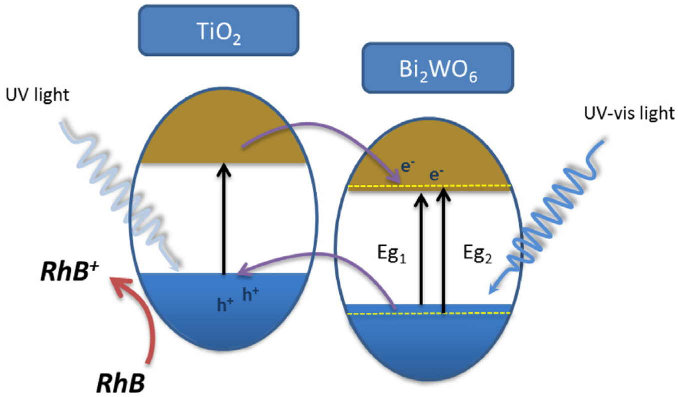

Scheme 1. Electronic flow upon UV–vis light excitation.

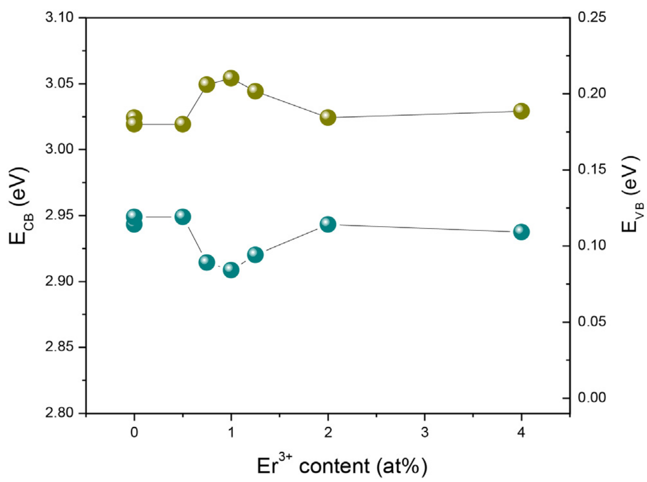

Fig. 7. Evolution of conduction and valence band edges (E_{CB} and E_{VB}) calculated from E_g for different Er^{3+} content.

to the photogenerated charge pairs, causing a better electron hole separation. This would explain the improved photoactivity under UV irradiation. Therefore, from this scheme, the contribution of a cooperative luminescence process could be discarded.

4. Conclusions

We have obtained a highly active TiO_2–Bi_2WO_6 system by doping with Er^{3+}. The hydrothermal synthesis leads to homogeneous heterostructured Bi_2WO_6 plate-like particles. From the structural and surface analysis the incorporation of Er^{3+} into the Bi_2WO_6 structure can be stated. The presence of Er^{3+} species produces a slight distortion of the russelite lattice. From the photocatalytic experiments under different irradiation conditions we tentatively propose a mechanism which could explain the improved photoactivities under UV irradiation in doped systems. The substitutionally incorporation of Er^{3+} into the Bi_2WO_6 structure would lead to a slight modification of the band structure. The slightly higher band gap values for lower doping levels would aid to the electron–hole separation under UV irradiation. Thus, Er^{3+} would help to the improved charge separation process, enhancing the UV-photoassisted process.

Acknowledgments

The financial support by projects *P09-FQM-4570* and *ENE2011-24412* is fully acknowledged. S. Obregón Alfaro thanks CSIC for the concession of a JAE-Pre grant.

References

[1] G. Colón, C. Belver, M. Fernández-García, in: M. Fernández-García, J.A. Rodríguez (Eds.), Synthesis, Properties and Application of Oxide Nanoparticles, Wiley, USA, 2007, ISBN 978-0-471-72405-6 (Chapter 17).
[2] A. Kubacka, M. Fernández-García, G. Colón, Chemical Reviews 112 (2012) 1555.
[3] X. Zhang, K. Udawa, Z. Liu, S. Nishimoto, C. Xu, Y. Lu, H. Sakai, M. Ave, T. Marakoi, A. Kujishima, Journal of Photochemistry and Photobiology A 202 (2009) 39.
[4] M.C. Hidalgo, M. Maicu, J.A. Navío, G. Colón, Journal of Physical Chemistry C 113 (2009) 12840.
[5] Y. Bessekhouad, D. Robert, J.V. Weber, Catalysis Today 101 (2005) 315.
[6] Q. Xiao, J. Zhang, C. Xiao, X. Tan, Catalysis Communications 9 (2008) 1247.
[7] H.G. Kim, P.H. Borse, J.S. Jang, E.D. Jeong, O.S. Jung, Y.J. Suh, J.S. Lee, Chemical Communications (2009) 5889.
[8] A. Kubacka, B. Bachiller-Baeza, G. Colón, M. Fernández-García, Journal of Physical Chemistry C 113 (2009) 8553.
[9] G. Colón, S. Murcia López, M.C. Hidalgo, J.A. Navío, Chemical Communications 46 (2010) 4809.
[10] C. Zhang, Y. Zhu, Chemistry of Materials 17 (2005) 3537.
[11] L. Zhang, W. Wang, L. Zhou, H. Xu, Small 3 (2007) 1618.
[12] X.C. Song, Y.F. Zheng, R. Ma, Y.Y. Zhang, H.Y. Yin, Journal of Hazardous Materials 192 (2011) 186.
[13] S.I. Naya, M. Tanaka, K. Kimura, H. Tada, Langmuir 27 (2011) 10334.
[14] S. Obregón, A. Caballero, G. Colón, Applied Catalysis B: Environmental 117–118 (2012) 59.
[15] S. Obregón, G. Colón, Chemical Communications 48 (2012) 7865.
[16] S. Obregon, A. Kubacka, M. Fernandez-Garcia, G. Colon, Journal of Catalysis 299 (2013) 298.
[17] M.C. Hidalgo, M. Aguilar, M. Maicu, J.A. Navío, G. Colón, Catalysis Today 129 (2007) 50.
[18] S. Obregón, S.W. Lee, G. Colón, Chemical Communications, submitted.
[19] M. Mączka, A.F. Fuentes, L. Kępiński, M.R. Diaz-Guillen, J. Hanuza, Materials Chemistry and Physics 120 (2010) 289.
[20] M. Mączka, J. Hanuza, W. Paraguassu, A.G. Souza Filho, P.T.C. Freire, J. Mendes Filho, Applied Physics Letters 92 (2008) 112911.
[21] M. Mączka, M. Ptak, L. Kępiński, P.E. Tomaszewski, J. Hanuza, Vibrational Spectroscopy 53 (2010) 199.
[22] Y. Zhou, E. Antonova, Y. Lin, J.D. Grunwaldt, W. Bensch, G.R. Patzke, European Journal of Inorganic Chemistry 2012 (2012) 783.
[23] M. Mączka, A.F. Fuentes, K. Hermanowicz, L. Macalik, P.E. Tomaszewski, L. Kępiński, R. Lisiecki, Journal of Nanoscience and Nanotechnology 10 (2010) 5746.
[24] S. Murcia López, M.C. Hidalgo, J.A. Navío, G. Colón, Journal of Hazardous Materials 185 (2011) 1425.
[25] L. Wu, J. Bi, Z. Li, X. Wang, X. Fu, Catalysis Today 131 (2008) 15.
[26] G. Wang, W. Qin, J. Zhang, J. Zhang, Y. Wang, C. Cao, L. Wang, G. Wei, P. Zhu, R. Kim, Optical Materials 31 (2008) 296.
[27] S. Murcia López, M.C. Hidalgo, J.A. Navío, G. Colón, Journal of Hazardous Materials 185 (2011) 1425.
[28] Y. Su, L. Hou, C. Du, L. Peng, K. Guan, X. Wang, RSC Advances 2 (2012) 6266.